

Simulation of Rotor-Rotor Interaction and Noise of an Axial Counter-Rotating Fan

I. Beldjilali¹, A. Ghenaiet^{2†} and L. Adjlout³

¹Energy Department, Faculty of Mechanical Engineering, University of Science and Technology Mohamed Boudiaf, BP 1505, Bir-El-Djir, 31000 Oran, Algeria

²Laboratory of Energy Conversion Systems, Faculty of Mechanical Engineering and Process Engineering, University of Science and Technology Houari Boumediene, BP32 El-Alia Bab-Ezzouar, 16111, Algiers, Algeria

³Department of Marine Engineering, Faculty of Mechanical Engineering, University of Science and Technology Mohamed Boudiaf, BP 1505, Bir-El-Djir, 31000 Oran, Algeria

†Corresponding Author Email: aghenaiet@usthb.dz

(Received October 5, 2022; accepted January 16, 2023)

ABSTRACT

The Counter-Rotating Fan (CRF) offers higher aerodynamic performance, in terms of pressure head and aerodynamic efficiency, compared to the single rotor fan, thus making it an attractive solution for equipment cooling and ventilation of mines and tunnels. Nevertheless, further investigations are required to understand the flow interactions between the front rotor (FR) and the rear rotor (RR), as these interactions are sources of noise emission. This numerical study used the Unsteady Reynolds Average Navier-Stokes (URANS) flow simulations and the Fast Fourier transformation (FFT) to analyse the rotor-rotor interactions and consequences on the aero-acoustic performance. The static pressure fluctuations were recorded at several locations and analysed by FFT to reveal the mechanisms of flow interactions and the effects of axial inter-distance between the two rotors. The inter-distance seems to influence the aerodynamic loading of RR more than that of FR and the total-to-static isentropic efficiency tends to drop. Over one chord distance, the noise level decreases but at the expense of isentropic efficiency. The balanced performance does not seem to improve for an inter-distance greater than 1.5 chords, considered the optimum distance in this study. Finally, a graphical correlation which can be used to estimate the Sound Pressure Level (SPL) is developed for this category of CRF.

Keywords: CRF; Aero-acoustic performance; Rotor-rotor interaction; Axial inter-distance; FFT.

NOMENCLATURE

BPF	Blade Passing Frequency	RR	Rear Rotor
c	chord	SPL	Sound Pressure Level
C	torque	SST	Shear Stress Transport
d	axial inter- distance	T	temperature
FR	Front Rotor	TE	Trailing edge
LE	Leading Edge	Z	Number of blades
N	rotational speed	URANS	Unsteady Reynolds Averaged Navier-Stokes
p	static pressure	x	axial distance
p_t	total pressure	ρ	density
Q_v	flow rate	η_{t-s}	total-to-static isentropic efficiency
r	radial distance from axis of rotation	ω	angular velocity
RANS	Reynolds Averaged Navier-Stokes	θ	observer angle

1. INTRODUCTION

Fans are vital devices widely used in many industrial fields. Fans with counter-rotation (CRF)

become a promising solution due to higher aerodynamic performance and lesser energy consumption (Lynam and Hawes 1946; Roy *et al.* 1992). However, the more stringent environmental regulations and comfort requirements have posed a

permanent challenge to the designers and pushed researchers to concentrate more on understanding the complex flows in order to reduce the noise emission (Mistry and Pradeep 2013; Romik and Czajka 2022). Indeed, the low-noise design is almost a systematic clause in the specifications submitted to the manufacturers to stand out from the competition (Wu *et al.* 2018).

One of the most challenging unsteady flow problems is the interaction phenomena in counter-rotating machines, which according to Dring *et al.* (1982), are sources of noise and vibrations. Higher efficiency and better aerodynamic stability could be achieved through an understanding of these common forms of unsteady flows arising from both periodic and non-periodic fluctuations (Macgregor 1990). Rotor-rotor interactions includes: the potential flow interaction and the wake interaction. In low speed fans, the effect of potential interaction is insignificant for an axial spacing more than 30% of blade pitch, while for the wake interaction, the trailing edge produces a velocity deficit in the flow field that convects downstream (Parker and Watson 1972). Meyer (1958) conducted the first study of wake blade interaction. He has described that as the wake arrives near the leading edge of the downstream blade the front part accelerates along the suction side away from the rear part that remains close to leading edge, and due to higher velocity on the suction side the wake exits the passage concentrated alongside with a tail reaching back to the pressure side. Later Binder *et al.* (1989) have concluded that the wakes of upstream blades are chopped by those at downstream, such that an avenue of wake pieces is generated which impacts the performance.

The noise comes primarily from the unsteady aerodynamic phenomena combined with the flow interactions between the moving and the fixed parts (Parry 1988). Jiang *et al.* (2007) studied experimentally and numerically the sound generation of an axial fan from a split type air-conditioner. Based on the code Fluent and the Fukano model (Fukano *et al.* 1977) they estimated SPL equal to 7.66 and 7.42 dB at 780 and 684 RPM, respectively, with an uncertainty around 10%. Despite their inaccuracy, the numerical simulations still have good opportunity to minimize the experimental costs. Moreau *et al.* (2006) obtained the complete sound spectrum of a low speed fan associated with the pressure fluctuations from the blades as obtained from URANS flow simulations.

For a CRF design it is therefore necessary to know the details of the mixing zone between the two rotors, especially the complex flow structure produced by the interaction of unsteady flows (Luan *et al.* 2018). The RR seems to influence more the aero-acoustic performance (Polacsek *et al.* 2006; Gao *et al.* 2014). Among the parameters affecting flow interactions is the inter-distance, which is a key-factor in reducing the noise (Holste and Neisser 1997). In this context, Brailko *et al.* (2004) developed a numerical approach to predict the noise produced by two counter-rotating rotors of the SV-27 propfan separated by an inter-distance of 650 and 950 mm, and have concluded that the emitted

noise and the acoustic pressure spectra are with good agreement with the experimental results. Schnell *et al.* (2012) performed aero-acoustic optimization of counter-rotating open rotors to maximize the aerodynamic efficiency in climb and to minimize the noise at takeoff condition. For this purpose, URANS solver was coupled with the analytical far field prediction method based on Ffowcs Williams and Hawkings (1969) (FW-H) noise model. Wu *et al.* (2018) investigated the noise of CRF considering URANS simulations and FW-H model, and by experiments they determined the peak of SPL around 500 Hz, which by increasing the inter-distance changed to the middle and low bands. Moreover, they indicated a peak value of the discrete noise in the low frequency region which reduced with the fan speed. Polacsek and Barrier (2007) presented a hybrid approach coupling URANS simulations with Computational Aero-Acoustics (CAA) codes of ONERA (Polacsek *et al.* 2006) to obtain the aero-acoustic characteristics of CRF model. The predicted SPL directivities indicate that the noise level is principally due to the rotor-rotor interaction. Also, Luan *et al.* (2016) investigated numerically the effect of inter-distance on the aero-acoustic performance of CRF, by solving the RANS equations with SST turbulence model under the design flow condition. As a result, the radiated noise at the characteristic frequency seems to decrease by increasing the inter-distance until an optimum equivalent to a half of chord. Later, Luan *et al.* (2018), based on URANS simulations, studied the rotor-rotor interactions and effects on the instability characteristics, and showed their importance to the aerodynamic performance of CRF.

This paper contributes to the study of the rotor-rotor flow interactions in a configuration of CRF, and their consequences on the aerodynamic loading of FR and RR and the overall performance of CRF. FFT analysis of the static pressure fluctuations recorded at different locations revealed the mechanisms of interactions and their sources. FW-H model was adopted to predict and derive a correlation between the noise level and the inter-distance between FR and RR.

2. STUDIED CRF AND CFD MODEL

The CRF configuration is composed of two counter-rotating rotors of the same geometry, shown in Fig. 1. Table 1 summarizes the main design parameters of the configuration tested previously by Ghenaïet and Beldjilali (2020).

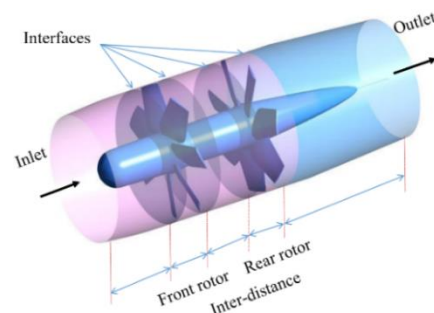


Fig. 1. CRF configuration.
Table 1 Design parameters of the CRF

Parameters	Value
Rotational speed N_{FR}	1440rpm
Rotational speed N_{RR}	-1440rpm
Maximum volume flow rate	$2.3\text{m}^3\cdot\text{s}^{-1}$
Chord(tip /hub)	(77.7/87.2 mm)
Hub diameter	78mm
Tip diameter	476mm
Stagger angle of FR	62 deg
Stagger angle of RR	67.4 deg
inter-distance	1.5chord

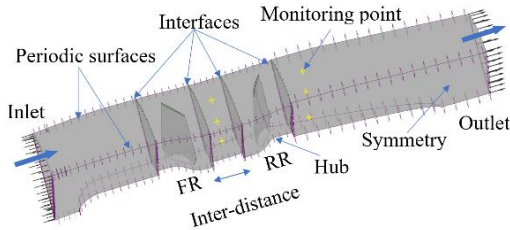


Fig. 2. Computational domain and boundary conditions.

The steady and unsteady solutions used the RANS and URANS equations and the $k-\omega$ based SST turbulence model under the commercial code ANSYS-CFX. To minimize the computation cost, the computational domain (Fig. 2) consists of one blade per passage. The inter-distance between two edges of the adjacent FR and RR blades refers to the mid-span.

The periodicity is applied at the lateral surfaces and the symmetry is at the axis of rotation. The first layer of nodes depends on the local Reynolds number Re_x and the overall Re_c according to $\Delta y = C y^+ \sqrt{80} Re_x^{-1/4} \frac{1}{Re_c}$. Figure 3 shows the values of y^+ which are within the accepted range, justifying the use of the wall law to perform the flow simulations. It is important to reduce the computation time and power during unsteady flows simulation without affecting the quality of the results. Preliminary simulations performed at the nominal operating conditions for different mesh sizes showed

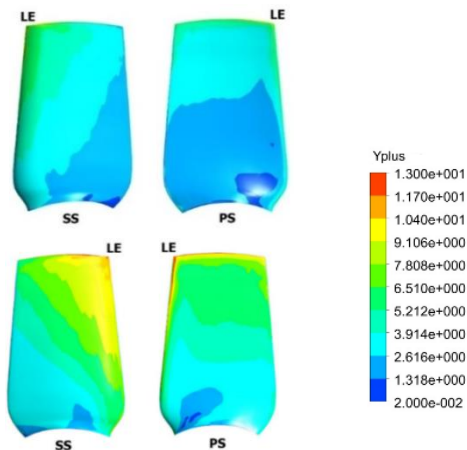


Fig. 3. y^+ over FR (top) and RR (bottom).

stabilization of the steady flow solution (Fig. 4) above the mesh size of 1028302 nodes and 975970 elements. Figure 5 depicts the actual meshes used.

3. STEADY FLOW SIMULATIONS

First, the RANS simulations were performed for the same tested CRF to ensure the validation of the CFD model. The most robust boundary conditions are imposed in terms of the total pressure of 101325 Pa and total temperature of 288.15 K at the inlet whereas the mass flow is at the outlet. The solver adopted the 2nd order Upwind Advection Scheme and an automatic time discretization and an RMS value of 10^{-6} . The mixed plane model “stage interface” is adopted in the steady flow simulations. This latter provides an alternative to the sliding mesh model for simulating flow through all the

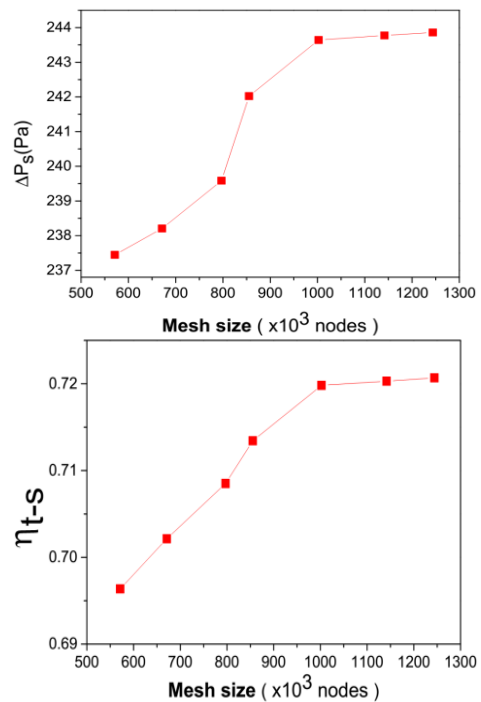


Fig. 4. Mesh size effect on static pressure rise (top) and total-to-static isentropic efficiency (bottom).

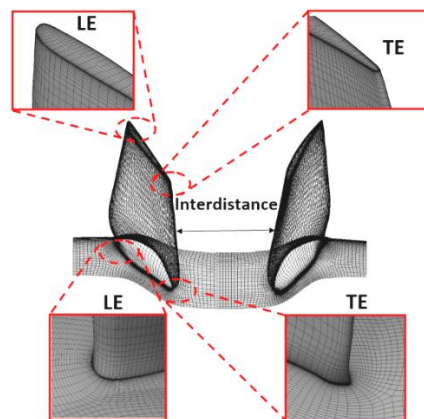


Fig. 5. Mesh quality.

domains with one or more regions in relative motion. The sliding mesh model may be appropriate, but in many situations, it is not practical to employ a sliding mesh (ANSYS-CFX-Solver Modelling Guide 2013). The essential idea behind the mixing plane concept is that each fluid zone is solved as a steady-state problem, and the flow-field data from adjacent zones are passed as boundary conditions that are spatially averaged in the circumferential direction or "mixed" at the mixing plane interface. Despite the simplifications inherent in this model, the resulting solutions can provide reasonable approximations of the time-averaged flow field.

Figure 6 shows that the computed static pressure rise and the total-to-static isentropic efficiency $\eta_{t-s} = \frac{Q_v \Delta p_{t-s}}{C \omega}$ agree with the experimental values, within the measurement uncertainties reported by Ghenaïet and Beldjilali (2020).

When the fan operates at a constant speed and the flow rate is continuously reduced, the angle of attack increases and the static pressure and the blade loading increase too. When exceeding the loading limit, large-scale separation and blocking occur and the efficiency drops (Gröwoldt Hesse and Sohn 2012). Below a limit flow rate, the vortices near the blade hub and at the tip cause a decrease in the flow angle and the work done by the blades, and therefore the pressure rise drops. As a result, the flow through the fan blades is not uniform, so the fan operates in an unstable state at low efficiency and high noise.

The inter-distance is an important parameter influencing aerodynamic performance. Figure 7 presents the total-to-static isentropic efficiency, showing that if the two rotors are close, they enter

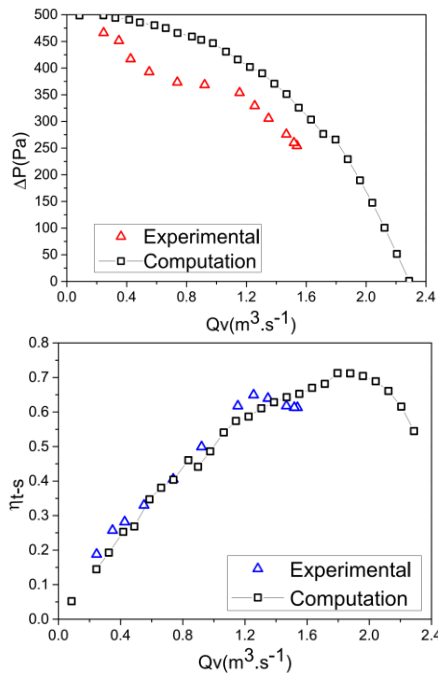


Fig. 6. Performance of CRF: static pressure rise (top); total-to-static isentropic efficiency (bottom).

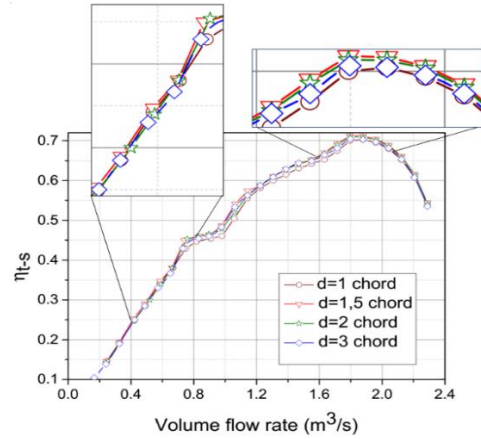


Fig. 7. Variation of total-to-static isentropic efficiency with inter-distance.

into significant flow interactions. As the inter-distance extends from 1 to 1.5 chords the total-to-static isentropic efficiency improves, but the contrary from 1.5 to 3 chords. At low flow rates, the total-to-static isentropic efficiency drops for the lowest inter-distance of 1 chord more than that for 3 chords. At the nominal condition, the total-to-static isentropic efficiency reaches the highest value at an inter-distance of 1.5 chords which seems the best setting to improve aerodynamic performance.

To reveal the effect of inter-distance on the aerodynamic loadings of FR and RR, the pressure coefficient $C_p = \frac{P - P_\infty}{\frac{1}{2} \rho_\infty V_\infty^2}$ (P static pressure over the

blade surface, P_∞ , ρ_∞ and V_∞ are the static pressure, density and air velocity of free stream conditions) is plotted at three spans of blade (15, 50 and 95 %) , according to Fig. 8. When CRF operates at the nominal condition (flow rate $Q_v = 1.87 m^3/s$), along the upper surface a depression region is visible, which is clearer in RR. It seems that the variation of inter-distance has insignificant effect on the pressure loading of FR, except a slight variation at 15 % of span for the smallest inter-distance of 1 chord. The pressure loading noticed at span 15 % becomes clearer at inter-distances of 2, 2.5 and 3 chords, successively.

In the region near the hub a depression zone is created due to secondary vortex caused by the recirculation. Due to variation of the inter-distance this depression influences the C_p in the blade region below 25% of span, and affects the flow angle of RR. In contrast, over 25%, the counter-rotation with an adequate flow angles allows reducing the shear of the fluid and conserving more total energy of the fluid of RR, and thus resulting in an increase of static and total pressure with more homogeneous flow at downstream till the blade tip.

The static entropy at mid-span (Fig. 9) reveals that the wake extension and the loss of kinetic energy localized from the trailing edge continues downstream. The closest distance of 1 chord has the highest entropy build-up since the wakes are not completely mixed, hence leading to lesser total-to-static isentropic efficiency.

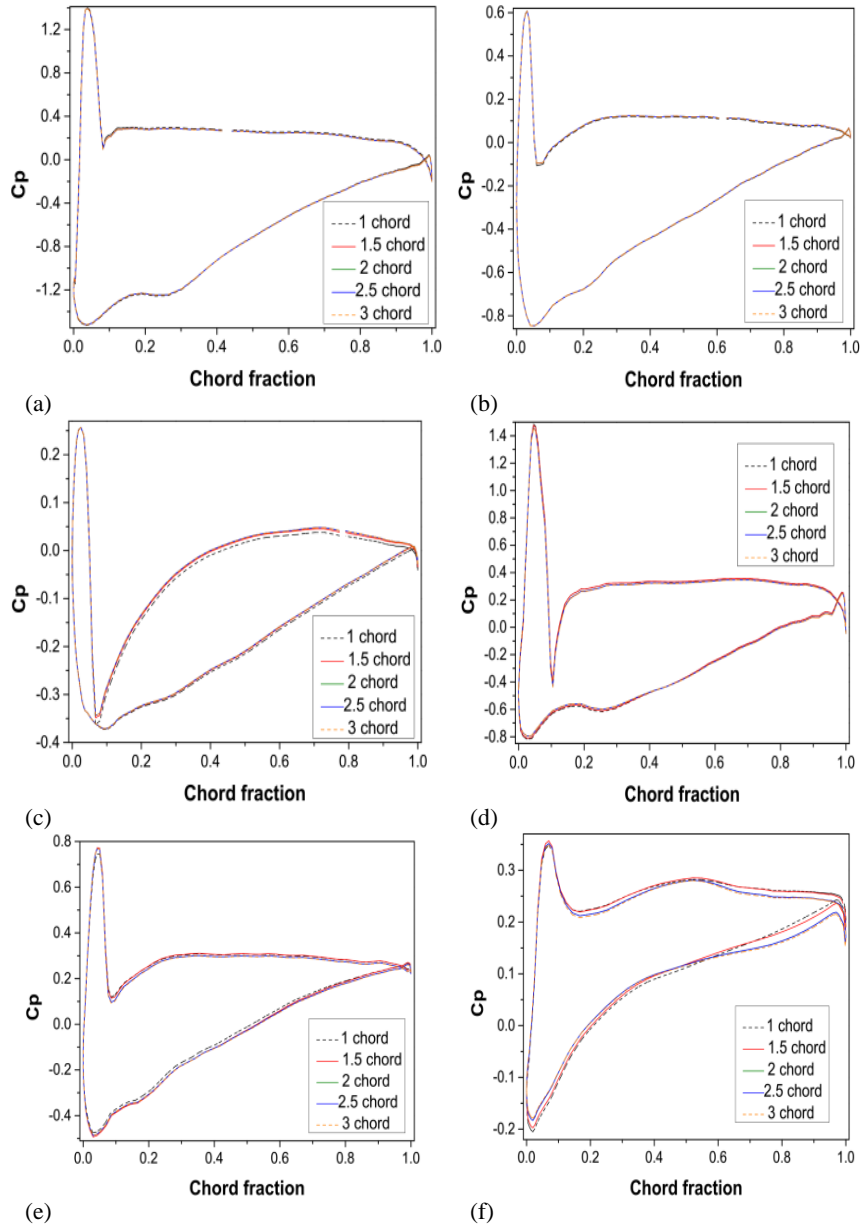


Fig. 8. Pressure loading: (a) FR at 95% span; (b) FR at 50% span; (c) FR at 15% span; (d) RR at 95% span; (e) RR at 50% span; (f) RR at 15% span.

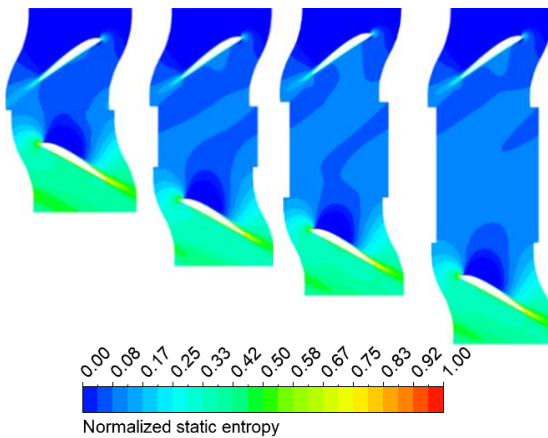


Fig. 9. Normalized static entropy at 50% span with inter-distance 1c, 2c, 2.5c and 3c, successively.

4. UNSTEADY FLOW SIMULATIONS

The computational domain reduced to one passage for each blade row (respecting the true periodicity) is supposed to represent the entire machine, and requiring lesser computation resources. The steady flow computations were performed based on the “Transient-Rotor-Stator” interface which accounts for transient interactions at the sliding (frame change) interface. With this approach the transient relative motion between the components on each side of the GGI connection is simulated, and ultimately accounts for all interactions effects between the components (ANSYS-CFX-Solver Modelling Guide 2013). The position of the interface is updated at each time step on the same time as the relative position of the meshes on each side of the interface varies.

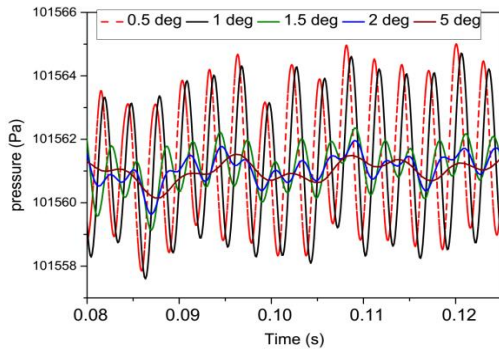


Fig. 10. Static pressure signal recorded at mid-span downstream of RR versus angle (time) step.

Theoretically, to have accurate results small time step has to be considered to obtain an adequate discretization, but higher computation power and power are required. Therefore, it is necessary to reduce these requirements without altering the quality of the results. The selection of the time step has led to investigating the time step dependency considering the fact that the solution should converge to an almost stationary pressure signals, considering the available computation resources. Touil and Ghenaïet (2019) performed unsteady flow simulations through a two-stage axial turbine by means of ANSYS-CFX with $k\omega$ based SST turbulence model. The transient rotor-stator interface was adopted and the time step was 0.789×10^{-5} second equivalent to 1 deg of blade advance. Younsi *et al.* (2016), for a CRF rotating at 2300 rpm, performed unsteady flow simulation using ANSYS-CFX and $k\omega$ based SST turbulence model based on the transient rotor-stator interface. A time step of 0.326×10^{-4} second equivalent to 2.22 deg was used, which led to good agreement between the

numerical results and the experimental results.

In this work, the preliminary assessment of five (time steps) angle steps between 0.5 - 5 deg allowed to make comparison between the pressure signals and their sensitivity upon the time step. Figure 10 shows different static pressure signals recorded at the point P5 (Fig. 15) for angle steps from 0.5 to 5 degree. As revealed, the pressure signals with 0.5 and 1 degree are practically identical. For the (time) angle step of 1 deg the time of computation took 6 days with i7-6820 HQ CPU 2.70 GHz with 32 Gb, while for the small time angle step of 0.5 degree, the computation cost was double. Accordingly, the time step of 1.157×10^{-4} second (angle step of 1 deg) was considered adequate when the high resolution transient scheme of the second order backward Euler was selected in the solver. The total time of simulation corresponded to three rounds of the rotor (equivalent to 0.125 second) and took about 6 days.

4.1 Flow Field Results

Figure 11 and Fig. 12 depict the temporal static pressure, while Fig. 13 and Fig. 14 show the normalized static entropy with inter-distance from 1 to 3 chords. Static pressure and entropy are chosen because they are independent from the reference frame and their azimuthal evolutions continue through the two rotors interface. The contours of the static pressure highlight the potential effects between the two blades rows. According to Fig. 11, if FR and RR are close, such as 1 chord, the potential effect is the strongest, in contrast to the farthest distance (Fig. 12). The interaction phenomena are mainly due to the wakes from the blades of FR chopped and damped by the mixing effects related to the RR blades rotation.

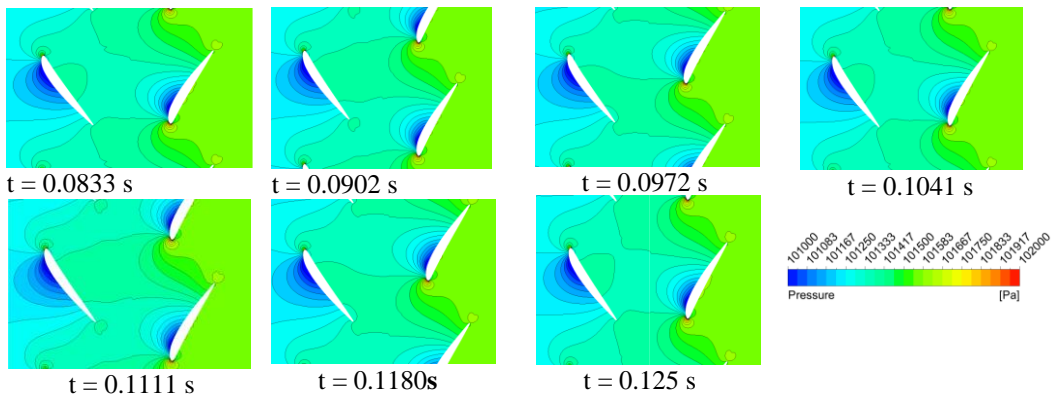


Fig. 11. Time evolution of static pressure at mid-span for d=1 chord.

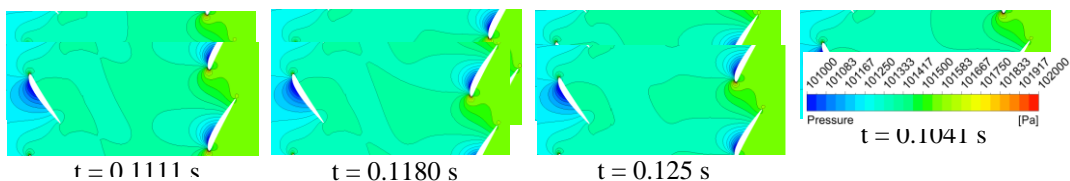


Fig. 12. Time evolution of static pressure at mid-span for d=3 chord.

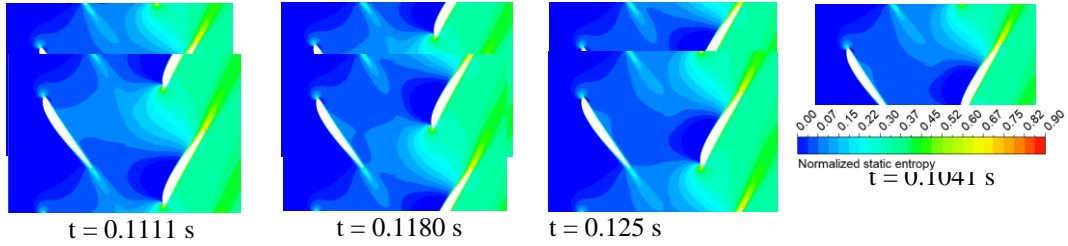


Fig. 13. Time evolution of normalized entropy at mid-span for d=1 chord.

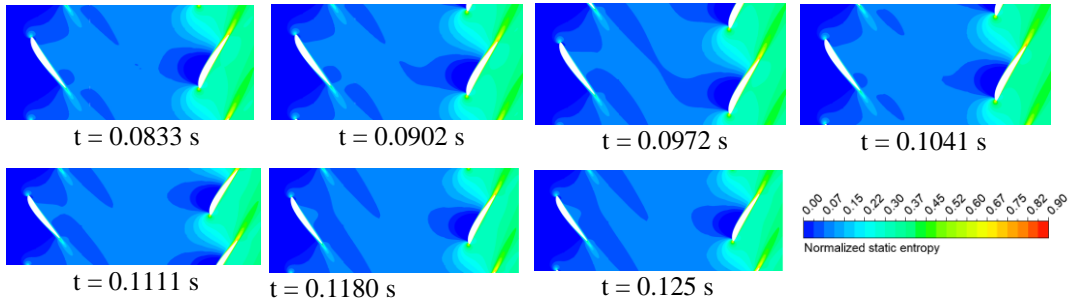


Fig. 14. Time evolution of normalized entropy of at mid-span for d=3 chord.

The contours of static entropy (Fig. 13-14) reveal the evolution of the interaction of the FR wake with the blades of RR. The static entropy distributions depict the losses intensity and reveal wakes and secondary flows convected into the RR blade. However, when the two rotors are close (1 chord), the entropy distribution changes drastically with evidence of large regions of losses characterizing the potential effects as the main source of losses, leading to a deficit in flow velocity with a circumferential distortion. For the largest inter-distance the interaction effects seem to decrease due to the wakes mixing between the blades rows.

4.2 Analyses of Flow Interactions

Flow unsteadiness in term of static pressure fluctuations allowed examining the interactions phenomena produced by the relative motion of the blades rows. The temporal static pressure were recorded at the points $P_1, P_2, P_3, P_4, P_5, P_6$ (Fig. 15) at 10, 50 and 95% of span, at the mid-distance between FR and RR and one chord downstream of RR. FFT analysis of the temporal pressure signals allowed the determination of the essential parameters characterizing these interactions, in terms of amplitude and frequency and evolution in time.

The sampling time step for the pressure signals recorded at points from P_1 to P_6 was specified to have a good accuracy in resolving the fundamental harmonics $BPF_1 = \frac{Z_{FR}}{60} N_{FR}$ and $BPF_2 =$

$\frac{Z_{RR}}{60} N_{RR}$ (N_{RR} in opposite direction) as well as detect the fluctuations smaller than the characteristic time step. Before using FFT it was necessary to eliminate unphysical and noise fluctuations. The following figures show the time pressure fluctuations (Fig. 16 to Fig. 20). As seen, the time interval to have the stabilization of pressure signals is from 0.083 to 0.126 s which corresponds to the third revolution. FFT spectrums depict the presence of a principal peak at the fundamental blade passing frequency (BPF) $f_1 = \frac{Z_{FR}}{60} N_{FR} = 168 \text{ Hz}$ for the two rotors. The magnitude of each fundamental frequency varies in the spanwise direction and from one recording plane to another (at mid-distance between FR and RR and at downstream of RR). The magnitudes of the principal peaks related to $f_3=336 \text{ Hz}$ are prevailing at the exit of FR for the one chord inter-distance (Fig. 16.a), but is damped through the RR until the exit. This frequency is also observed at the exit of RR for both 2.5 and 3 chords (Fig. 16.b and 16.c), but at lower pressure

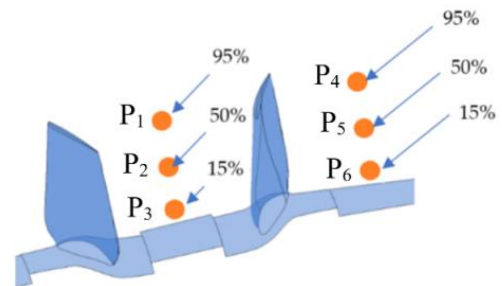
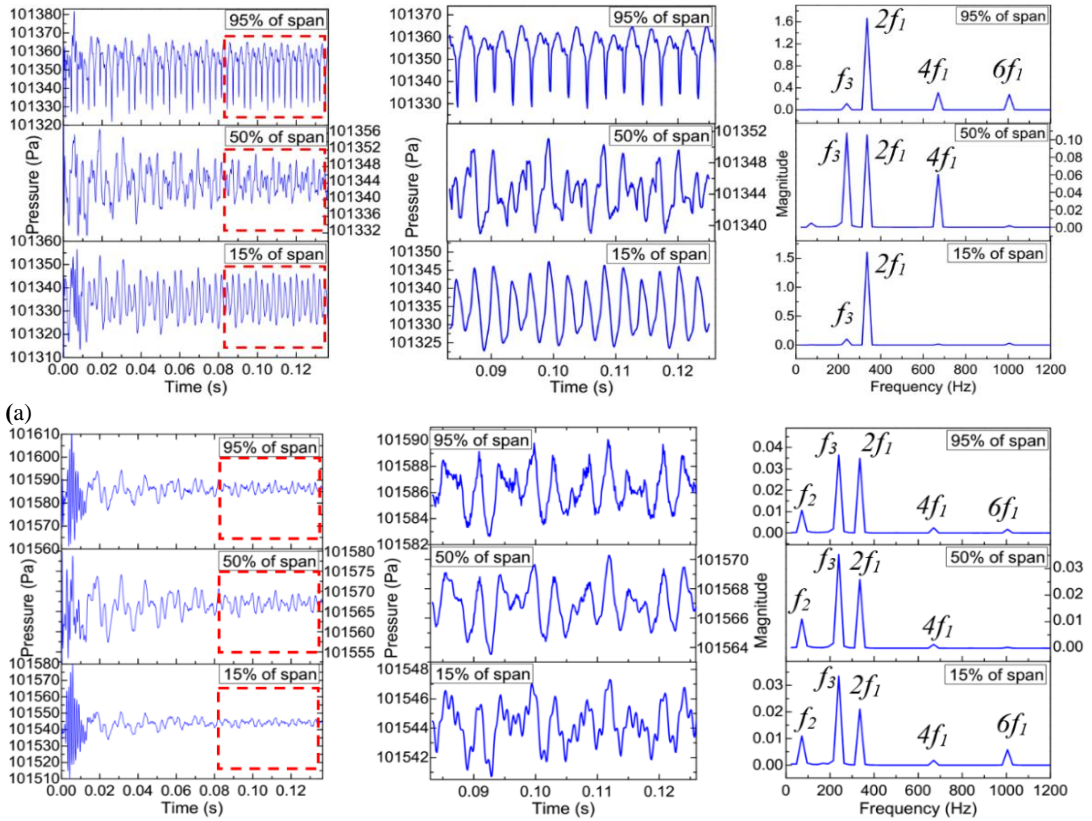
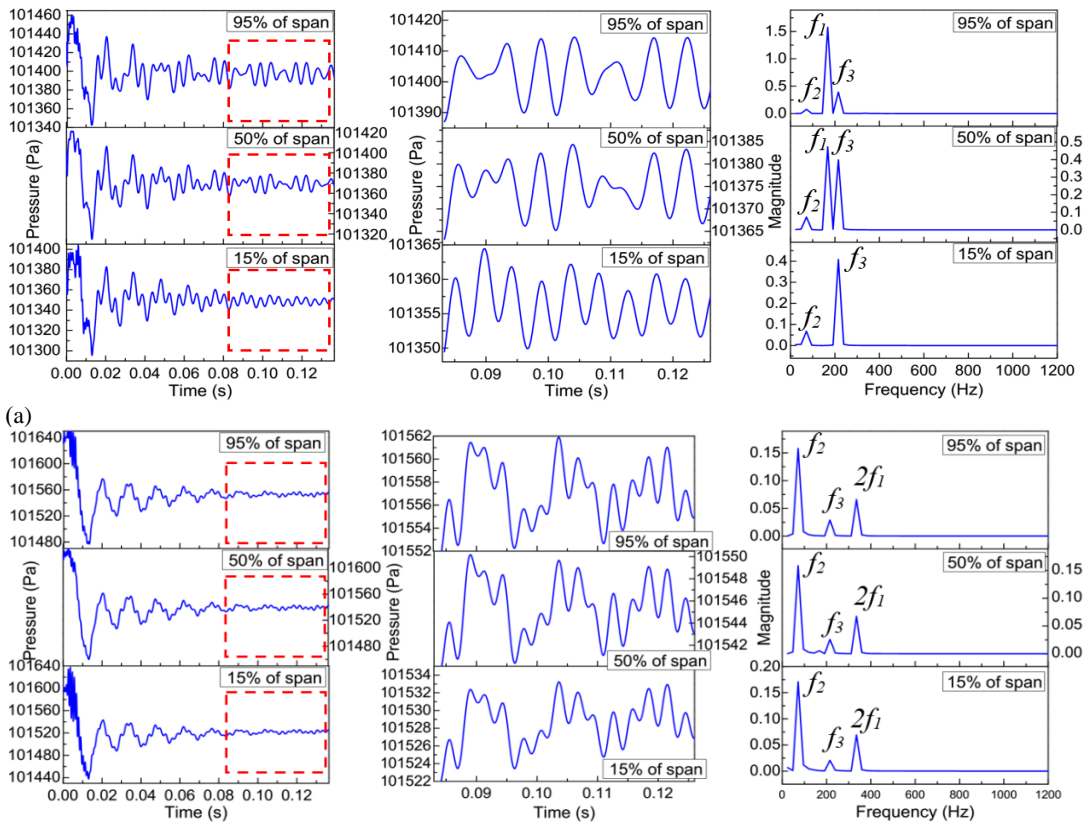


Fig. 15. Recording points.



(b) **Fig. 16. Temporal pressure fluctuations and FFT at 15, 50 and 95% of span and for inter-distance of 1 chord at: (a) mid distance; (b) downstream of RR.**



(b) **Fig. 17. Temporal pressure fluctuations and FFT at 15, 50 and 95% of span and for inter-distance of 1.5 chords at: (a) mid distance; (b) downstream of RR.**

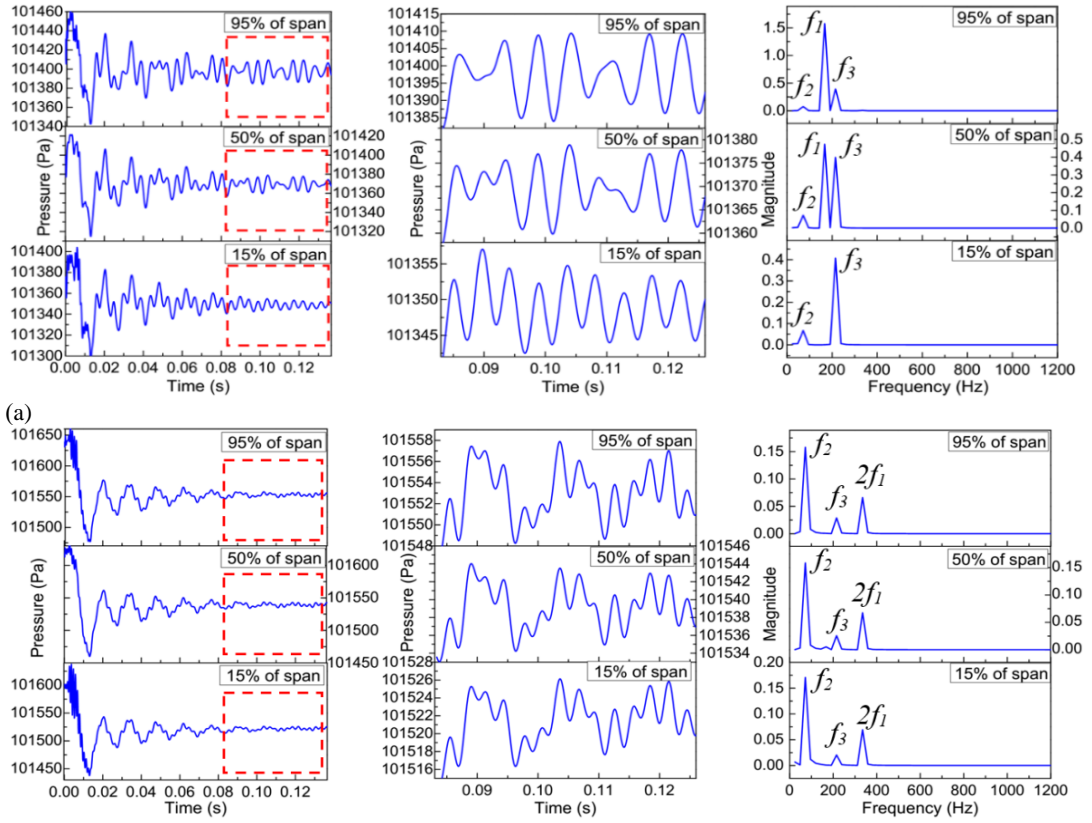


Fig. 18. Temporal pressure fluctuations and FFT at 15, 50 and 95% of span and for inter-distance of 2 chords at: (a) mid distance; (b) downstream of RR.

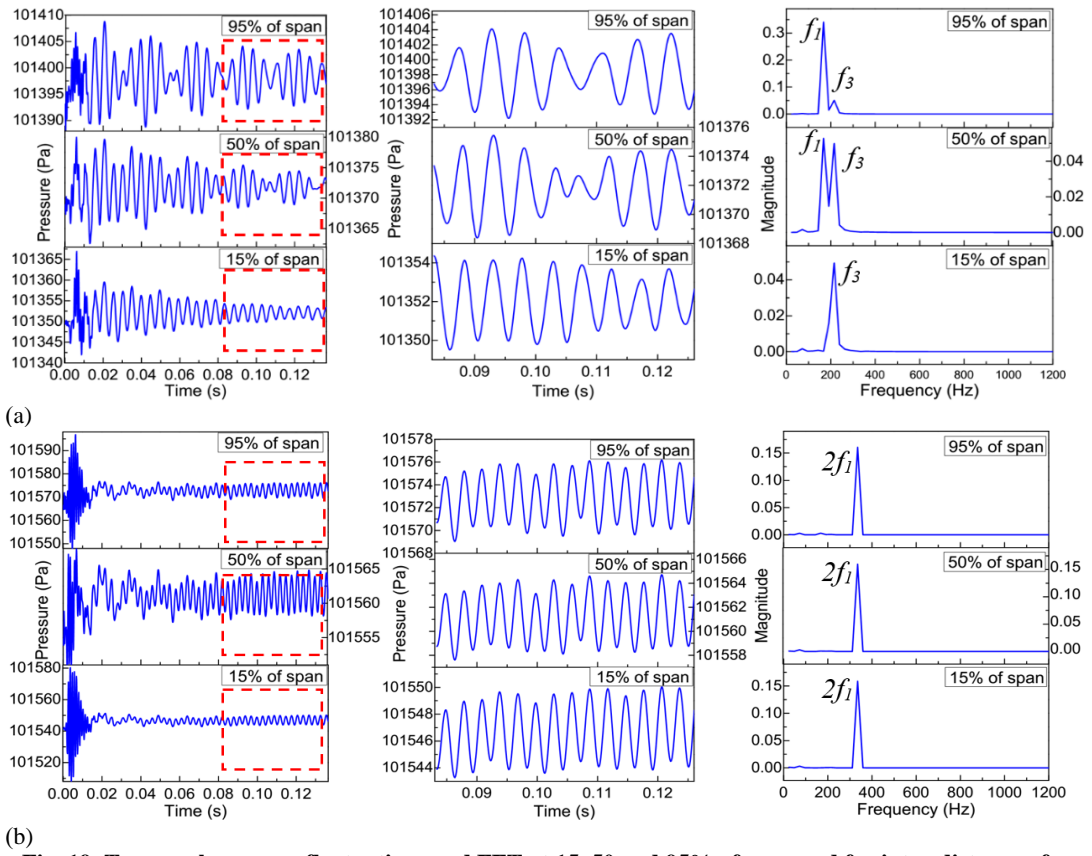


Fig. 19. Temporal pressure fluctuations and FFT at 15, 50 and 95% of span and for inter-distance of 2.5 chords at: (a) mid distance; (b) downstream of RR.

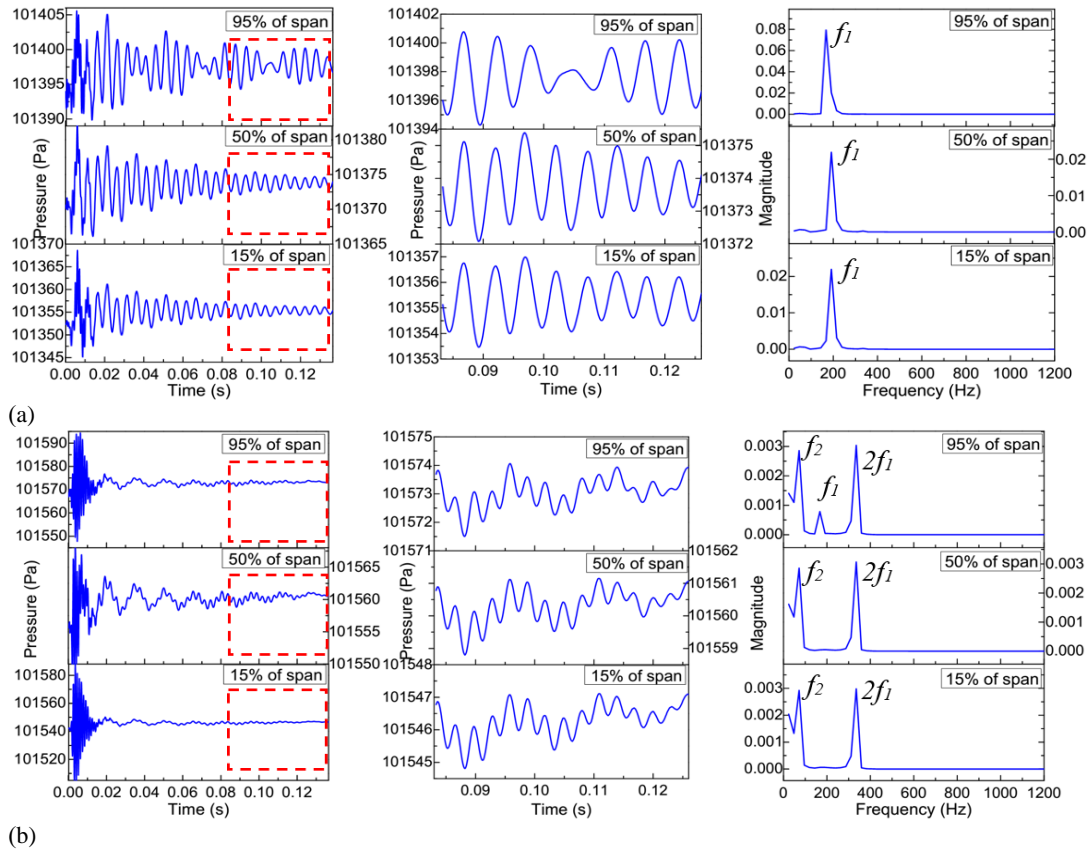


Fig. 20. Temporal pressure fluctuations and FFT at 15, 50 and 95% of span and for inter-distance of 3 chords at: (a) mid distance; (b) downstream of RR.

amplitudes from 3 to 8 Pa, hence leading to very small amplitudes in FFT. Likewise, there is emergence of other frequencies such as 239 Hz dominant at exit from RR for 1 chord inter-distance (Fig. 16.b), with another frequency of $f_2 = 72$ Hz for 1.5 chords (Fig.17.b), 2 chords (Fig.18.b), and 3 chords (Fig.19.b), respectively. These two frequencies seem related to the vortices formation from the blade tip and trailing edge. Figure 16 reveals another dominant frequency ($2f_1$) and harmonics which shows the effect of RR on the static pressure field in-between the two blades rows. Downstream of RR, there is dominance of the frequency f_2 . FFT spectrums in Fig. 19 and Fig. 20, reveal that the static pressure fluctuation of the two rotors is dominated by the frequency f_1 in-between the two rotors and only by $2f_1$ downstream RR which seems affected by the pressure wave of FR.

The increasing of axial inter-distance has a significant impact on the pressure fluctuation amplitudes, reaching a maximum value when the two rotors are close enough. When the rotors are closely spaced (1 chord), the internal flow field begins to deteriorate, and the phenomena of inlet vortex, flow channel vortex, boundary layer vortex, and rotational stall occur. At this condition, the high fluctuation is due to the interactions between the rotors which led to complex phenomena of large-scale vortex structure. With the increase of inter-distance the internal flow of the CRF is more regular than at close distance, in addition, the stress and strain of the second rotor blade are stable. The

pressure fluctuations in the middle of blades rows and downstream RR depict slight changes and the frequency pattern of the pressure pulse shows a more regular pattern. Downstream of RR the pressure amplitudes increase in the first time up to an inter-distance of 2 chords and then decrease for higher inter-distances.

Furthermore, the fundamental frequencies resulting from the linear combination of the first and the higher order between the fundamental frequencies cannot appear clearly in all the recorded points. This may be due to other complex flow phenomena related to the formation of vortices having their speed of rotation. To get better insight, it is required to multiply the number and positions of recording points in the spanwise and circumferentially directions, in addition to other points on the blades to monitor the loading fluctuations and the torque oscillation.

5. NOISE ASSESSMENT

The noise was simulated on the computational model using a large eddy combined with sound simulation based on the FW-H model (Ffowkes Williams and Hawkings 1969). The far-field noise of CRF was determined by calculating the time-domain integral and area fraction. The time required was $\Delta t = 1.1574 \times 10^{-4}$ second equivalent to 1 deg of rotor angle step. The sound field was calculated by FFT to determine the sound pressure SPL. The formula for solving the time domain for the

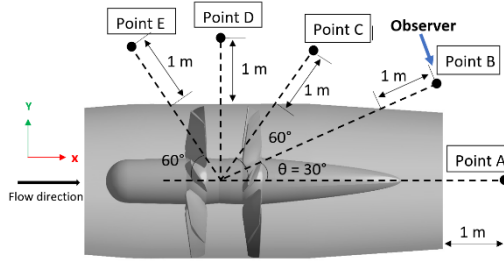


Fig. 21. Noise reception points.

instantaneous sound pressure \dot{p} is according to Wu and Yi (2021):

$$\dot{p} = \frac{1}{4\pi} \int_{f=0} \left(\frac{\dot{L}_r}{r^2} \right) dS + \frac{1}{4\pi} \int_{f=0} \left(\frac{\dot{L}_r}{r^2} \right) dS \quad (1)$$

In equation (1) $L_r = L_i \hat{r}_i$ and $\dot{L}_r = \dot{L}_i \hat{r}_i$ where the dot represents the time derivative. $L_i = p n_i$, n_i is the wall normal vector. r the distance from the sound source to the receiving point. \hat{r}_i represents the unit vector from the sound source to the receiving point. The speed of sound is equal to the standard value of 340.17 m/s.

Based on the equation (1) the sound pressure level (SPL) is given according to Fukano *et al.* (1977) as follows:

$$SPL = 10 \log_{10}(\bar{p}^2/p_{ref}^2) \quad (2)$$

Where $p_{ref} = 2 \times 10^{-5} \text{ N/m}^2$ chosen so that in a perfectly free field at a distance where the propagation surface is 1 m^2 , the sound pressure and sound power levels are identical.

Figure 21 depicts the five recording positions surrounding the CRF, and respecting some criteria defined in the standards (GB/T2888-2008), according to Luan *et al.* (2016). The point A is at a distance of 1 m from the exit of CRF, whereas the points B, C, D and E are placed at a distance of 1 m from the fan duct at angles of 30, 60, 90 and 120 deg, respectively.

In Fig. 22 and Fig. 23, the SPL levels are presented at each point for an axial spacing from 1 to 3 chords. For the FR the inter-distance does not seem to clearly influence SPL. Indeed, SPL reaches its maximum at the machine axis for the value of 61.91 dB at point A, whereas for the RR, it is noticed that for an inter-distance of 1 chord, the SPL has a maximum value of 49.7 dB at point A. One may conclude that SPL decreases by increasing the inter-distance for each control point.

Domain FR

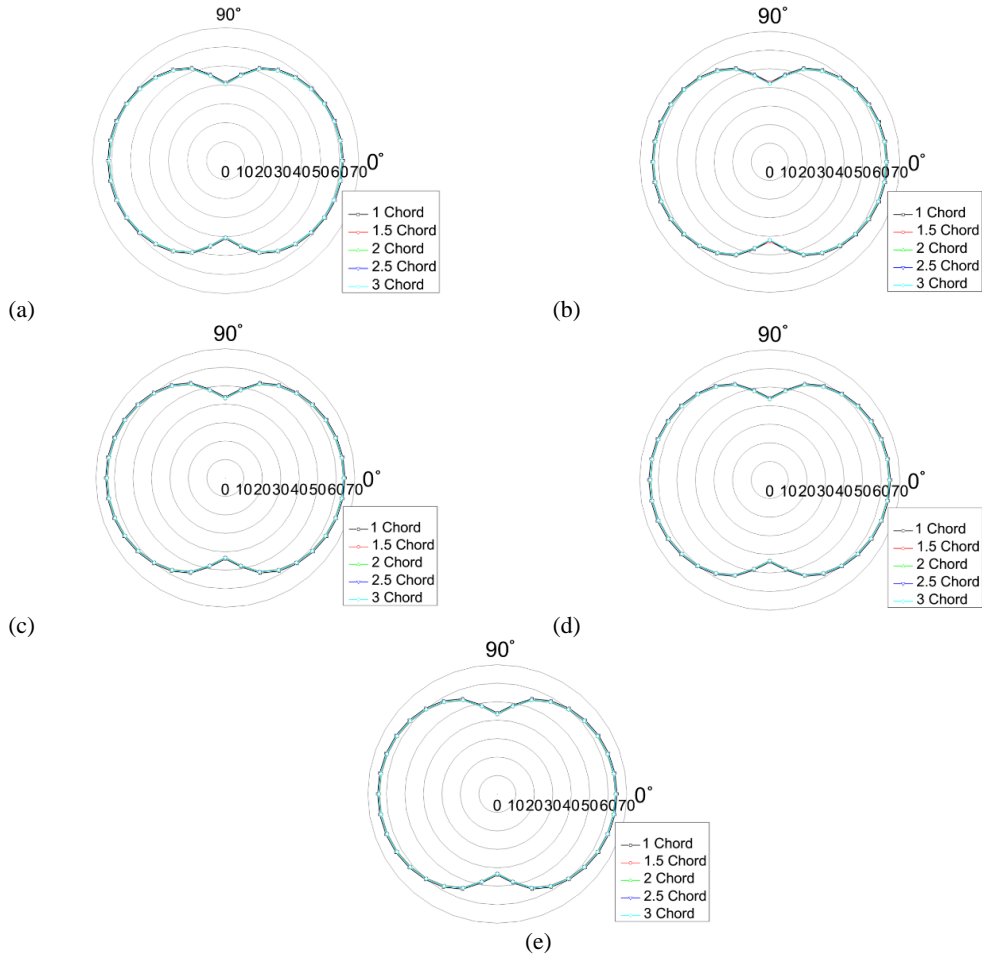


Fig. 22. SPL of FR in XY plane with inter-distance: a) point A, b) point B, c) point C, d) point D, e) point E.

Domain RR:

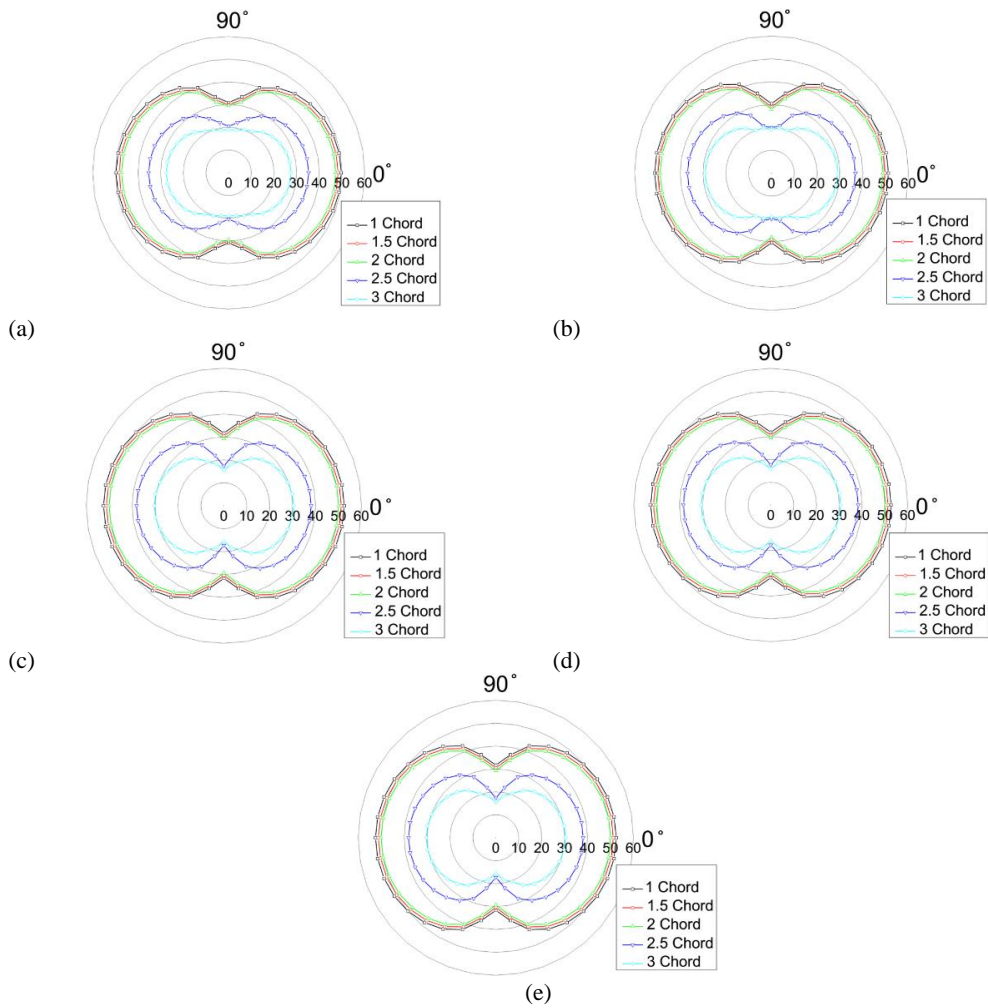


Fig. 23. SPL of RR in XY plane with inter-distance: a) point A, b) point B, c) point C, d) point D, e) point E.

When designing CRF it is also important to select an axial spacing leading to the highest isentropic efficiency at a reasonable noise level. Indeed, the aerodynamic performance, particularly the isentropic efficiency, seems to decrease for larger axial spacing while the noise level reduces. Indeed, Fig. 24 shows that by increasing the inter-distance

from 1 to 3 chords SPL drops but at the expense of isentropic efficiency. At the farthest axial spacing of 3 chords the SPL reaches its lowest value. One may conclude that around an inter-distance of 1.5 chords this CRF configuration may achieve the best aerodynamic efficiency with an acceptable noise level.

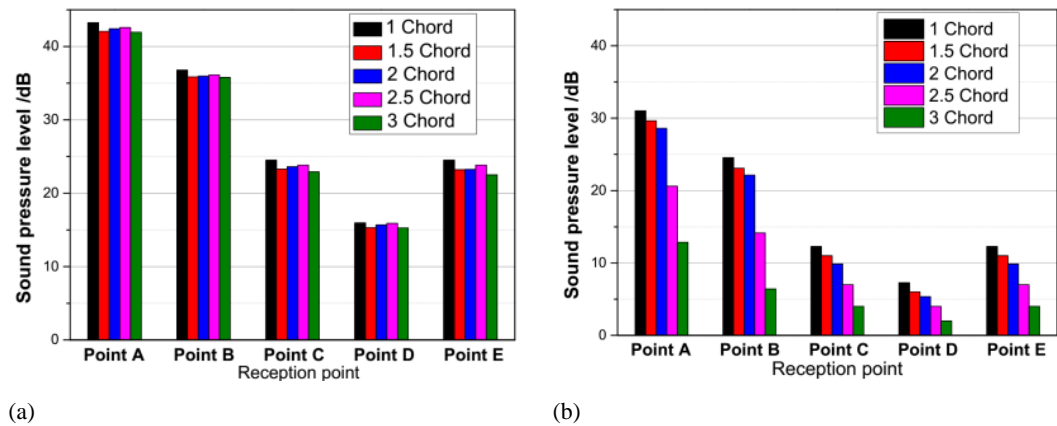


Fig. 24. Influence of inter-distance on SPL: a) FR, b) RR.

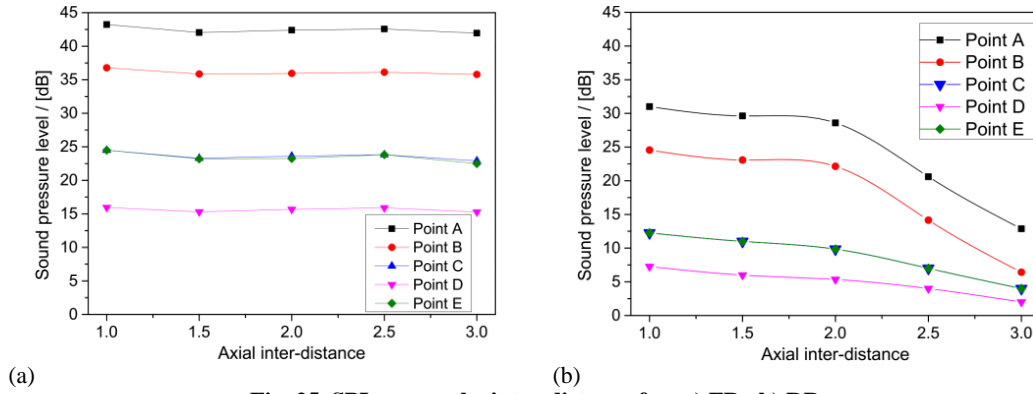


Fig. 25. SPL versus the inter-distance for: a) FR , b) RR.

A correlation is derived, relating the acoustic propagation at any given position, function of the axial spacing x and observation angle θ . Figure 25 illustrates the evolutions of SPL of FR and RR as a function of inter-distance normalized by the mean chord of the blade. Figure 25.a shows that the axial distance does not affect the SPL of the FR, which the maximum is attained for 1 chord and equal to 43.3 dB for the point A. On the other side, the RR (Fig. 25.b) seems to produce a lower noise level compared to FR, and depicts significant variations with inter-distance, where SPL curve first show a slight decrease up to the distance of 2 chords and then drops significantly above.

Accordingly, the SPL of FR is correlated against the inter-distance as follows:

$$SPL = a_4 d^4 + a_3 d^3 + a_2 d^2 + a_1 d + a_0 \quad (3a)$$

The coefficients $\alpha_{i=0,1,2,3,4}$ are function of the observer angle θ (radian) and are provided in Table 2:

$$\alpha_{0,1,2,3,4} = \lambda_3 \theta^3 + \lambda_2 \theta^2 + \lambda_1 \theta + \lambda_0 \quad (3b)$$

Table 2 Coefficient α_i for FR.

	λ_3	λ_2	λ_1	λ_0
α_0	2.509	0.256	-31.142	81.938
α_1	27.374	-81.707	76.117	-76.143
α_2	-24.136	70.098	-62.086	52.468
α_3	8.642	24.535	21.026	-15.408
α_4	-1.089	3.029	-2.535	1.633

The SPL of RR is correlated similarly, where the coefficients $\alpha_{i=0,1,2,3,4}$ function of the observer angle θ (radian) are provided in Table 3:

Table 3 Coefficients for RR.

	λ_3	λ_2	λ_1	λ_0
α_0	90.821	-248.850	64.328	185.390
α_1	-190.060	530.010	-161.870	-347.950
α_2	159.020	-443.090	135.701	282.630
α_3	-56.304	156.830	-48.354	-97.825
α_4	7.017	-19.544	6.070	11.961

To assess the uncertainty in noise prediction, Christophe *et al.* (2013) compared the experimental results for the noise of a low-speed single fan with the results obtained from the URANS computations considering the $k\omega$ based SST turbulence model within the code ANSYS-CFX. As a result, they found the uncertainty in SPL of the far-field noise about 2 - 6 dB. Based on the same commercial software and solver settings, one would assume that the current uncertainty of predicted SPL could be in the same range.

6. CONCLUSION

The present work investigated the steady and unsteady flow interactions through a configuration of CRF, which the CFD model was validated against test results. FW-H model was adopted to simulate the noise propagation. The main findings are enumerated as follows:

- The rotor-rotor interaction has significant effects on the unsteady flow field
- The upstream wakes seem to enhance the energy exchange between the boundary and the main stream, and hence suppress the flow separation.
- The effect of inter-distance on the pressure loading is more obvious for the RR blade for the closest inter-distance.
- At the closest inter-distance the aerodynamic performance drops slightly, whilst the optimum is obtained for 1.5 chords.
- When the rotors are too close, high fluctuations in static pressure are due to the flow interactions leading to complex phenomena, such as the vortex flows and mixing as well as the large-scale vortex structure ruptures.
- After attaining the maximum value at the closest inter-distance between FR and RR, the pressure fluctuations decrease for larger inter-distances. Also, the pressure fluctuations downstream of RR start to decrease for more than 2 chords.
- The inter-distance seems to affect the SPL of RR more than the FR.

- SPL decreases slightly from 1 to 2 chords and significantly at 3 chords, where the lowest noise level was recorded. This is mainly due to the damping of the wakes with the inter-distance.
- Finally, the inter-distance of 1.5 chords seems to provide better performance while keeping an acceptable noise level.

A better understanding of the two rotors coupling is needed by adding more recording points over the blades to monitor the loading fluctuations and torque oscillations. Also, carry out an optimization of aero-acoustic performance involving the blades setting and axial spacing.

REFERENCES

- ANSYS CFX-Solver Modeling Guide, Release 15.0, November 2013, ANSYS, Inc., Canonsburg, PA15317
- Binder, A., T. Schröder and J. T. Hourmouziadis (1989). Turbulence measurements in a low-pressure turbine. *ASME Journal of Turbomachinery* 111, 153-161.
- Brailko, I. A., V. I. Milesin, M. A. Nyukhtikov and S.V. Pankov (2004, July). Computational and experimental investigation of unsteady and acoustic characteristics of counter-rotating fans. In *Heat Transfer Summer Conference*, Charlotte, North Carolina, USA
- Christophe, J., M. Sanjose, S. Moreau, J. A. Witteveen, and G. Iaccarino (2013). Uncertainty quantification of low-speed fan noise. In *19 th AIAA/CEAS Aeroacoustics Conference*.
- Dring, R. P., H. D. Joslyn, L. W. Hardin and J. H. Wagner (1982). Turbine rotor-stator interaction. *ASME Journal of Engineering for Power* 104, 729, 1982b.
- Ffowcs Williams, J. E. and D. L. Hawkings (1969). Sound generated by turbulence and surfaces in arbitrary motion. *Philosophical Transactions of the Royal Society of London* A264, 321-342.
- Fukano, T., Y. Kodama and Y. Senoo (1977). Noise generated by low pressure axial flow fans, I: Modeling of the turbulent noise. *Journal of Sound and Vibration* 50(1), 63-88.
- Gao, L. M., F. Miao, R. Y. Li and B. Liu (2014). Effect of rotor/rotor interactions on blades unsteady loading. *Acta Aeronautica et Astronautica Sinica* 35(7), 1874-1881.
- Ghenaiet, A. and I. Beldjilali (2020). Influence of staggering and inter-distance on performance of a low-speed counterrotating axial fan. *Journal of Aerospace Engineering* 33(1), 04019109.
- Polacsek, C., S. Burguburu, S. Redonnet and M. Terracol (2006). Numerical simulations of fan interaction noise using a hybrid approach. *AIAA Journal* 44(6), 1188-1196.
- Gröwoldt Hesse, H. and A. G. Sohn (2012). Stall and parallel operation. In *6th International Conference Tunnel Safety and Ventilation*, Gratz.
- Holste, F. and W. Neise (1997). Noise source identification in aPropfan model by means of acoustical near field measurements. *Journal of Sound and Vibration* 203(4), 641-665.
- Jiang, C. L., J. P. Chen, Z. J. Chen, J. Tian, H. Ou Yang and Z. H. Du (2007). Experimental and numerical study on aeroacoustic sound of axial flow fan in room air conditioner. *Applied acoustics* 68(4), 458-472.
- Luan, H., L. Weng and Y. Luan (2018). Numerical simulation of unsteady aerodynamic interactions of contra-rotating axial fan. *Plos One* 13(7), e0200510.
- Luan, H., L. Weng, Y. Luan, Y. Zhang and P. Chen (2016). Numerical study on aerodynamic noise performances of axial spacing in a contra-rotating axial fan. *Journal of Vibroengineering* 18(8), 5605-5618.
- Lynam, F. C. and S. P. Hawes (1946) *Contra Rotating Axial Flow Fans*. The Engineers.
- Macgregor, J. D. (1990). *Three Dimensional Viscous Flow Model of Stator/Rotor Interaction in Turbomachines*, Ph.D. thesis, Texas A&M University.
- Meyer, R. X. (1958). The effect of wakes on the transient pressure and velocity distribution in turbomachines. *ASME Journal of Basic Engineering* 80, 1544-1552.
- Mistry, C. and A. M. Pradeep (2013). Effect of variation in axial spacing and rotor speed combinations on the performance of a high aspect ratio contra-rotating axial fan stage. In *Part A: Journal of Power and Energy*, 227, 2.
- Moreau, S., M. Henner, D. Casalino, J. Gullbrand, G. Iaccarino and M. Wang (2006). Toward the prediction of low-speed fan noise. In *Proceedings of the summer program (Vol. 9)*, Center for Turbulence Research.
- Parker, R. and J. F. Watson (1972). Interaction effects between blade rows in turbomachines. *Proceedings of the Institution of Mechanical Engineers* 186, 331-340.
- Parry, A. B. (1988). *Theoretical Prediction of Counter-Rotating Propeller Noise*. PhD Thesis, University ofLeeds.
- Polacsek, C. and R. Barrier (2007). Numerical simulation of counter-rotating fan aeroacoustics. In *13th AIAA/CEAS Aeroacoustics Conference (28th AIAA Aeroacoustics Conference)*.
- Romik, D. and I. Czajka (2022). Numerical investigation of the sensitivity of the acoustic power level to changes in selected design parameters of an axial fan. *Energies* 15(4),

1357.

Roy, B., K. Ravibabu, P. S. Rao, S. Basu, A. Raju and P. N. Murthy (1992). Flow studies in ducted twin-rotor contra-rotating axial flow fans. In *Turbo Expo: Power for Land, Sea, and Air*. American Society of Mechanical Engineers.

Schnell, R., J. Yin, C. Voss and E. Nicke (2012). Assessment and optimization of the aerodynamic and acoustic characteristics of a counter rotating open rotor. *Journal of Turbomachinery* 134(6), 061016.

Touil, K. and A. Ghenaïet (2019). Simulation and analysis of vane-blade interaction in a two-stage high-pressure axial turbine. *Energy* 172,

1291-1311.

Wu, C. and Z. Yi (2021). Research on aerodynamic noise of tandem double cylinders based on k-fwhsound comparison method. *Journal of Beijing University of Aeronautics and Astronautics* 2021, 47(10).

Wu, J., Z. Kou and J. Liu (2018). The acoustical behavior of contra-rotating fan. *Mathematical Problems in Engineering*, ID 3739067.

Younsi, M., B. Hutchinson, F. Ravelet, S. Khelladi, and F. Bakir (2016). Numerical simulation of the unsteady aerodynamics in an axial counter-rotating fan stage. In *12th International Conference on Heat Transfer, Fluid Mechanics and Thermodynamics*.